UNITED NATIONS UNIVERSITY
UNU-WIDER
World Institute for Development Economics Research

WIDER Working Paper No. 2013/040

Regional climate change of the greater Zambezi River Basin

A hybrid assessment

C. Adam Schlosser and Kenneth Strzepek*

April 2013

Abstract

Projections of regional changes in seasonal surface-air temperature and precipitation for the eastern and western Zambezi River Basin regions are presented. These projections are cast in a probabilistic context based on a numerical hybridization technique of the MIT Integrated Global System Model. Unconstrained emissions send the majority of outcomes in spring precipitation to a drying by 2050, although the total distribution spans both precipitation increases and decreases. From climate policy, the distributions' range collapse considerably and the distributions' mode lies near zero precipitation change. For surface air temperature, the most notable effect of climate policy is to reduce the mode value of warming as well as the occurrence of the most extreme increases.

Keywords: Zambezi, regional, climate, change, risk
JEL classification: Q54, Q25

* Massachusetts Institute of Technology, Joint Program on the Science and Policy of Global Change, corresponding author email: casch@mit.edu

This study has been prepared within the UNU-WIDER project on Development under Climate Change, directed by Channing Arndt, James Thurlow, and Finn Tarp.

UNU-WIDER gratefully acknowledges the financial contributions to the research programme from the governments of Denmark, Finland, Sweden, and the United Kingdom.

ISSN 1798-7237 ISBN 978-92-9230-617-5

Acknowledgments

The presented analyses for the Zambezi River Basin were funded by United Nations University—World Institute for Development Economic Research (UNU-WIDER). The authors gratefully acknowledge this as well as additional financial support for this work provided by the MIT Joint Program on the Science and Policy of Global Change through a consortium of industrial sponsors and federal grants. Development of the IGSM applied in this research was supported by the U.S. Department of Energy, Office of Science (DE-FG02-94ER61937); the US Environmental Protection Agency, EPRI, and other US government agencies and a consortium of 40 industrial and foundation sponsors. For a complete list see http://globalchange.mit.edu/sponsors/current.html.

Figures appear at the end of the paper.

UNU World Institute for Development Economics Research (UNU-WIDER)
Katajanokanlaituri 6 B, 00160 Helsinki, Finland

Typescript prepared by Lisa Winkler at UNU-WIDER.

1 Introduction

Growing demands for climate change vulnerability assessments and adaptation strategies have placed a need for risk-based quantification of regional change. Considerable attention has been directed toward developing nations where the capability to make informed decisions and/or capital investments based on climate risk are at a premium. In this study, we present analyses for the greater Zambezi River Basin (ZRB) that quantifies the likelihood of changes in precipitation and surface air temperature through the middle of this century. These probabilistic climate outcomes have been prepared for an integrated assessment of the anticipated economic shocks to the basin from climate change and other socio-economic forces. In the section that follows, we present this approach, which includes the construction of an observation-based climatology of the downscaling patterns as well as a normalization of the climate model patterns of regional change. These steps are based on global climate model (GCM) ensemble results from the Intergovernmental Panel on Climate Change (IPCC) Fourth Assessment Report (AR4). The resulting frequency distributions are evaluated for a select number of regions to assess their consistency with the inferred distributions from the more limited sample of the IPCC model collection, and further analyses evaluates the shifts in these derived distributions under a moderate climate stabilization policy. Closing remarks and directions for future work *and* applications are then provided.

2 Characterizations of regional climate shifts

2.1 Greater Zambezi River Basin

The greater ZRB (white shaded area in Figure 1) is our area of focus for this risk-based assessment of regional climate change. Within the chain of climate impact models and the regional computable general equilibrium (CGE) model of Mozambique, the two main climate variable inputs are precipitation and near-surface air temperature (T_a). The impact models are configured to resolve the major sub-basins and demographic regions of the basin, and the climate variables are provided at a 2˚x2˚ grid resolution. Overall, this region of southern Africa is characterized by a robust seasonal hydro-climate. The warmest temperatures over the basin are experienced along the border of Zambia and Zimbabwe (Figure 2). The coolest temperatures lie just to the north over interior sections of Zambia. Over most of the basin, a modest seasonal swing in temperature is experienced and is in the order of 4 ˚C, with the strongest seasonality within the interior portions of the basin in Zambia. Perhaps most interesting in the temperature record is that the path of the Zambezi River appears to follow along the stretch of warmest temperatures with a notably buffered seasonality.

In contrast to temperature, the ZRB experiences a widespread and robust seasonality of precipitation (Figure 3). A very notable and ubiquitous dry season occurs during June-August. During this time the most depleted rates of precipitation are found over the western ZRB (denoted by the WZRB) labeled boxes in Figures 2-4) where most of the area experience average precipitation rates of less than 0.05 mm/day. The situation improves slightly for the eastern ZRB (denoted by the EZRB labeled boxes in Figures 2-4), where precipitation rates increase to 0.5-1.0 mm/day along the coastal area of the Mozambique Channel. This hydro-climatic situation takes a dramatic turn during December-February in that much of the ZRB experiences precipitation rates in excess of 5 mm/day, with a notable

portion subjected to precipitation in excess of 8 mm/day. During March-May, the northern flank of the basin experiences sizable precipitation rates (in excess of 2 mm/day), whereas in September-November, the remnants of the dry season are somewhat persistent and only the north-western most portion of the basin has begun to experience inflated precipitation. Nevertheless, the September-November season is quite important, agriculturally speaking, given that it coincides with the time of planting. Given these distinct seasonal characteristics of the basin, the subsequent analyses will, accordingly, present diagnoses of the potential changes in these climate variables by 2050.

2.2 Regional climate change pattern kernels

The construction of our presented frequency distributions of climate changes follows that of previous work (Schlosser et al. 2011). The probabilistic projections of T_a and precipitation out to the middle of this century are provided at the zonal level of detail by the MIT Integrated Global Systems Model (IGSM) (Sokolov et al. 2009; Webster et al. 2011). However, given that the atmospheric outputs IGSM are at the zonal level detail, we expand in the longitude through a Taylor expansion technique (described by Schlosser et al. 2012). This transformation requires the construction of climate change pattern kernels as the global temperature changes, and the numerical relationship can be expressed as:

$$V_{x,y}^{IGSM}(\Delta T_{Global}) = C_{x,y}\Big|_{t_0} \overline{V}_y^{IGSM} + \left[\frac{dC_{x,y}}{dT_{Global}} \Delta T_{Global}^{IGSM}\right] \overline{V}_y^{IGSM} \quad (1)$$

where $C_{x,y}\Big|_{t_0}$ is the downscaling transformation coefficient (from the zonal mean down to a longitudinal point along the zonal band) for any reference time period, and in our case, we can base this on a climatological set of values, $\overline{C}_{x,y}$, based on observational data. Accordingly, ΔT_{Global} is the (projected) change in global temperature that has occurred relative to the reference or climatological period. Then, based on supporting data the derivative of these transformation coefficients, $\frac{dC_{x,y}}{dT_{Global}}$, for any point (x,y) must be estimated (for further details on the construction of these, refer to Schlosser et al. 2012). Therefore, the regional specificity of the climate change probabilities is governed, in large part, by the $\frac{dC_{x,y}}{dT_{Global}}$ terms that serve as 'pattern kernels' of regional climate shifts. A set of these pattern kernels is based on the results from the IPCC AR4 (IPCC 2007), and we present a summary of these below.

Precipitation

The model mean of $\frac{dC_{x,y}}{dT_{Global}}$ for precipitation (Figure 4) indicates that the most notable (relative) shifts in regional precipitation will occur during spring (September-November), as seen by the widespread negative $\frac{dC_{x,y}}{dT_{Global}}$ values—indicating a relative drying (with respect to the zonal mean) over the region as global climate warms. During the summer months (December-February), this situation is replaced with small positive values over the western

ZRB, but the negative values persist over much of the eastern ZRB. Only during the fall (March-May) does the eastern basin see a notable portion with positive values of $\frac{dC_{x,y}}{dT_{Global}}$ (indicating a relative increase in precipitation with climate warming). It should be noted that with respect to the zonal trends in precipitation that the IGSM produces in response to increased greenhouse gas concentrations. The region experiences a diverse range of zonal precipitation trends (see Figure 9 of Schlosser et al. 2012). Over the northern flank of the basin, the majority of the zonal precipitation trends are positive, while in the southern flank the sign of the zonal precipitation trends are equally distributed. This will, undoubtedly, factor considerably into the resulting frequency distributions of precipitation change for the basin (presented in later sections). To an equal extent, the range of precipitation change patterns from each of the AR4 climate models also display diverse textures. During spring (Figure 5), a few of the models exhibit enhanced drying over most of the basin, while the remaining models show a buffered drying extent. During summer (Figure 6), the diversity among the models is even more pronounced; with a few models producing widespread enhanced precipitation patterns, while other models will impose enhanced widespread drying. The remaining models show a mixture of drier or wetter precipitation conditions (relative to the zonal trend) as climate warms.

Temperature

In contrast to precipitation, the results of $\frac{dC_{x,y}}{dT_{Global}}$ for T_a (Figure 7) show a strong, consistent characterization that resembles the colder ocean and warmer land global pattern (e.g., Broccoli et al. 1998). In terms of the model mean response, this pattern is persistent for all seasons, with a small degree of migration of the relative maxima of change. In terms of the zonal mean trends, the IGSM produces a fairly consistent zonal profile of warming over the region (see Figure 8 of Schlosser et al. 2011). Therefore, these patterns will essentially enhance the zonal warming (as the global climate warms) over the entire ZRB. However, the extent of the enhanced regional warming will be affected by the choice of the pattern kernel, as evidenced by the scatter of these patterns amongst the AR4 models (Figures 8 and 9). For most of the AR4 models, the pattern kernels will produce a stronger regional warming enhancement during spring than in summer—as seen by the expansive, higher values of $\frac{dC_{x,y}}{dT_{Global}}$ during September-November (Figure 8). However, most of the models' pattern kernels place the area of strongest regionally enhanced warming to the south or just along the southern flank of the ZRB (Figure 1). Yet as indicated in the model mean pattern (Figure 7), during spring there is a notable number of models that extend the strongest warming into the western river basin. During summer, this sub-basin enhancement is less prevalent among the models' patterns with only a couple of the models showing a salient feature in this regard.

2.3 Hybrid frequency distributions

Through the numerical hybridization of the IGSM ensemble of zonal trends with each of the pattern kernels of regional climate change from the IPCC AR4 models, a meta ensemble of climate change projections is produced, and hereafter we refer to as 'hybrid frequency distributions' (HFDs). For this presentation, we focus on the decadal averaged climate conditions that are achieved at 2050 and construct frequency distributions of the changes in

precipitation and T_a relative to the end of the 20th century. Decadal averaged results are provided in order to highlight the salient features of the climate scale changes (and remove effects of weather-scale noise). In addition, given the distinct seasonal characterizations of the regional climate change pattern kernels, and the importance of the spring and summer climate conditions as inputs to the agricultural impact models used for any larger integrated study, we focus on the distributions obtained during the September-November (SON) and December-February (DJF) averaging periods. The IGSM ensembles produce a range of climate outcomes under an unconstrained emissions pathway (Sokolov et al. 2009) as well as a range of global climate policies (Webster et al. 2011). In the interest of clarity, we focus on a subset of these climate projections. We present results for the unconstrained emissions (UCE) case and a modest greenhouse gas stabilization scenario in which an equivalent CO_2 concentration of ~650 ppm is achieved by the end of the century—and is referred to as the 'Level 2 stabilization' (L2S) policy in Webster et al. (2011).

Western Zambezi River Basin

Looking at the UCE case, the resulting HFDs of the area-averaged T_a changes for SON (Figure 10) indicate that the mode of the temperature-change distribution to be in the 2.0˚C - 2.25˚C range by 2050. The distribution shows a fairly robust Gaussian shape, but with a slight skewness toward higher temperature increases. This skewness is consistent with some of the AR4 models' pattern kernels imposing a stronger warming over the sub-basin (Figures 7d and 8). The impact of the L2S climate policy is a modest reduction in the mode warming by about 0.75˚C, but more notably, the entire L2S distribution of warming lies at or below the bottom half of the UCE distribution. As a result, the highest warming of the L2S distribution coincides with the mode warming of the UCE distribution. Further, over 70% of the L2S distribution lies at or below a 1.5˚C warming, whereas only 7% of UCE distribution occurs at or below this warming. Perhaps the more striking impact of the climate policy scenario is seen in the SON precipitation results (Figure 11). Under the UCE pathway, the western ZRB exhibits a fairly broad range of outcomes, the span both decreases and increases in precipitation. However, the mode of precipitation change (with just over 20% of the distribution) lies rather saliently within decreased precipitation and is in the range of -0.2 to -0.1 mm/day (note in Figure 11 values are presented in units of mm/decad, with decad = 10 days). What is equally striking in the UCE distribution is the rather broad tail in the distribution that result in precipitation increases as high as 0.7 to 0.8 mm/day and decreases as low as -0.6 mm/day. The effect of the L2S climate policy scenario on the HFD is considerable. The new mode value is half the value seen in the UCE case, and now contains 55% of the distribution. However, The L2S distribution still places nearly as much of the distribution (~20%) for the mode value of the UCE, but the long tailed features of the UCE distribution are not seen for the L2S case. Overall, less than 1% of the L2S distribution exceeds a -0.2 mm/day reduction or 0.2 mm/day increase in precipitation (as opposed to ~40% and 8%, respectively, for the UCE scenario).

For the summer months (DJF), the shape and response of the HFDs for the two scenarios considered bear a striking resemblance to that of spring for T_a change, but notable differences are seen for precipitation. For the UCE scenario, the mode value of the DJF T_a changes is the same as that of spring (SON); with a mode value of temperature increase is 2.0˚C to 2.5˚C (Figure 12). For precipitation change (Figure 13), the most densely populated portion of the distribution flanks the result of no change. However, there is a slight skewness in that 57% of the distribution results in increased precipitation, with 43% indicating a decrease. Further, the largest precipitation increases are greater in magnitude than the corresponding decreases. The

impact of the L2S scenario primarily reduces the occurrence of the most extreme precipitation changes (both positive and negative), and the most extreme outcome is about 50% to that of the UCE (Figure 13). As a result, the increase in the portion of the population flanking no precipitation change is considerable, with nearly 45% of the population as opposed to 28% in the UCE. For T_a, the effect is similar but somewhat weaker to that seen in the summer months. The reduction in the mode warming is 0.5˚C, and much of the L2S population resides in the lower half of temperature warming seen in the UCE scenario. However, there is a small portion of the L2S population (~3%) that remains in the upper half of the warming outcomes of the UCE. In either scenarios, nearly all of the ensemble member population results in a 1.0 ˚C warming by 2050.

Eastern Zambezi River Basin

The HFDs for T_a changes in the summer months for the eastern Zambezi show the weakest response to climate policy among all the cases considered herein. The mode value of temperature increase is 1.25˚C to 1.5˚C (Figure 14) and is comprised of 30% of the ensemble member population. The effect of the L2S policy scenario is subtle with a slight decrease in the mode value (0.25˚C), and the mode now contains 37% of the ensemble-member population. In addition, a slight reduction is seen in the maximum warming outcomes and their occurrences (Figure 14). Generally speaking, the L2S distribution is close to the result one would obtain by taking the UCE distribution and shifting it along the abscissa by -0.25˚C. For DJF precipitation changes, similar to the features noted for the western Zambezi region (seen in Figure 13), the more densely populated regions of the HFDs in both scenarios considered lie quite close to the result of zero precipitation change by 2050 (Figure 15). Nevertheless, the skewness of the tails of the distribution as well as their shifts in response to the L2S climate policy are notable. For the UCE case, 60% of the distribution results in increased precipitation, and the highest increases in precipitation exceed in magnitude any of the lowest decreases. The L2S scenario places an equal percentage of the population in both decreases and increases in precipitation (Figure 15). In addition, the occurrence of the most extreme precipitation increases is almost completely removed and a considerable portion of the larger increases in precipitation are buffered. This results in a more salient modal feature of the distribution, which surrounds a result of the no precipitation change. Moreover, the occurrence of extreme decreases or increases in precipitation is almost equally likely.

During spring, the HFDs for T_a changes exhibit a consistent behavior as seen in the cases thus far. However, in this case we find the lowest modal value of temperature increase compared to any of the distributions presented in this study, with a value of 1.0˚C to 1.25˚C (Figure 16). This result is consistent with the fact that geographically, this region may be more affected by its proximity to the Mozambique Channel and the onshore fetch of the larger ocean thermal inertia. This consideration may also apply to the fact that the most extreme temperature increases for the eastern Zambezi region for SON and DJF are at least 1.0˚C lower than those seen for the western Zambezi region. Nevertheless, the impact of the L2S policy is discernable. Although the decrease in the mode value of temperature warming is small, only a 0.25˚C decrease in the warming, the increase in the portion of the population that resides in the mode is considerable (Figure 16). The L2S contains nearly 43% of the distribution in the mode value of warming (0.75˚C to 1.0˚C) as opposed to 25% for the UCE scenario. Similar to that found for the western Zambezi region, the features and shifts for SON precipitation change in both the UCE and L2S are among the most striking. For the UCE case, the mode of the distribution indicates a decrease in precipitation, with 40% of the ensemble-member population flanking a value of -0.15 mm/day (Figure 17). As a result, the majority of the

population (91%) projects decreased precipitation. However, the HFD exhibits very broad tails that span both decreases and increases in precipitation, yet only 9% of the population results in increased precipitation. The effect of the L2S scenario is similar to that found in the western Zambezi and is considerable. The total range of precipitation changes encompassed by the HFD is compressed by over a factor 3 (from 10 mm/decad to 3 mm/decad). Most notably, however, is that over 75% of the distribution lie in the two bins that flank zero precipitation change. One of these is the mode value, -0.05 to 0.0 mm/day, with over 45% of the population residing in it.

3 Closing remarks

We have presented results from a numerical hybridization technique that provides a probabilistic survey of the potential climatic shifts in precipitation and near surface air temperature over the greater ZRB. The results are presented as HFD that are based on a core ensemble of simulations with the MIT IGSM of an unconstrained emissions pathway and a modest climate policy scenario aimed to limit greenhouse gas concentrations by the end of this century. These simulations are combined with 'climate change pattern kernels' based on results from the IPCC AR4 climate model collective, and results in a meta ensemble of potential climate outcomes. These hydro-climatic outcomes are used as inputs into regional impact models of agricultural productivity, infrastructure damage, as well as a CGE model of the Mozambican economy. A synopsis of the climate change pattern kernels and the HFDs is provided in support of any further impact-assessment work.

The climate change pattern kernels show a robust spatial consistency across all seasons, and indicate that over the ZRB the warming is enhanced with respect to the zonal trend provided by the IGSM. This is consistent with previous analyses with climate models indicating a 'colder ocean, warmer land' feature prevalent in most climate change projections. For precipitation, a majority of the region, on average, should experience an enhanced drying with respect to the zonal trend. However, this generalization is somewhat misleading in that the individual climate change kernels exhibit a rich variety in the locations of drier and wetter conditions. Further, there is a notable seasonality in the patterns, which indicates the strongest relative drying to occur in the spring over most of the region. Nevertheless, the resulting changes in precipitation and surface air temperature are a result of the fusion of the pattern change kernels and the zonal IGSM trends.

The resulting projections from the regional constructions are presented by averaging the precipitation and T_a changes over the western and eastern Zambezi regions. In addition, results for the spring and summer seasons presented given their importance to agricultural productivity and that these seasons, climatologically speaking, contain the highest precipitation rates. Overall, the most significant response to climate policy is seen in the distributions of spring precipitation change. In both basins, the unconstrained emission HFDs indicate a majority of the outcomes to result in a drying by 2050, although the distribution also covers a wide range of changes and span increased and decreased precipitation. Through the climate policy considered, the HFDs' total range of outcomes collapse considerably, and perhaps more importantly, the modal portion of the distribution becomes aligned with zero precipitation change. For summer precipitation, the most salient feature to the climate policy impact is to reduce the occurrence of the largest precipitation changes (both increases and decreases), thereby condensing the total width of the distribution outcomes. These shifts result in an increase in the portion of the population that resides in the modal value, however the modal value does not change considerably. For surface air temperature, the most

consistent impact of climate policy is to reduce the mode value of warming, and this reduction is strongest for the distributions of the western Zambezi region. Climate policy primarily abates the occurrence of the most extreme temperature increases, and thus the resulting minimum warming that is encompassed by these distributions is less affected.

Overall, quantifiable risks of these climate change distributions can only be enabled through explicit vetting of these data through a chain of impact models. Future work will consider the thinning of the large size of these meta-ensembles (6,800 members per scenario) according to a Gaussian quadrature technique (e.g., Arndt et al., 2006) that reduces the total ensemble size while preserving the more important hydro-climatic aspects of the distribution. These can then be applied to the hydrologic simulations of the region in support of assessing crop productivity impacts. While these linkages described convey a one-way flow of climate information into these impact models, ultimately, the overall goal of this research endeavor is to provide the regional environmental and economic information back into the larger scale global economic and earth system models of the IGSM framework.

References

Arndt, C., Kozlitina J., and Preckel P.V. (2006). 'Efficient survey sampling of households via Gaussian quadrature'. *J Royal Stat Soc: Series C* (Applied Statistics), 55: 355-64.

Broccoli, A.J., Lau N.C., and Nath M.J. (1998). 'The cold ocean–warm land pattern: Model simulation and relevance to climate change detection'. *J Climate*, 11: 2743-63.

Huffman G J, Adler RF, Bolvin DT, Gu G (2009) Improving the global precipitation record: GPCP Version 2.1. Geophys Res Let 36:1-5. http://www.agu.org/pubs/crossref/2009/2009GL040000.shtml

IPCC (2007) Summary for policymakers. In: Solomon S, Qin D, Manning M, Chen Z, Marquis M, Averyt KB, Tignor M, Miller HL (eds) Climate change 2007: the physical science basis. Contribution of Working Group I to the Fourth Assessment Report of the Intergovernmental Panel on Climate Change. Cambridge University Press, Cambridge, UK and New York

Jones PD, New M, Parker DE, Martin S, Rigor IG (1999) Surface air temperature and its variations over the last 150 years. Reviews of Geophysics 37:173-199

Schlosser CA, Gao X, Strzepek K, Sokolov A, Forest C, Awadalla S, Farmer W (2011) Quantifying the likelihood of regional climate change: A hybridized approach. *J. Climate,* doi: 10.1175/JCLI-D-11-00730.1.

Sokolov AP, Stone PH, Forest CE, Prinn R, Sarofim MC, Webster M, Paltsev S, Schlosser CA, Kicklighter D, Dutkiewicz S, Reilly J, Wang C, Felzer B, Jacoby HD (2009) Probabilistic forecast for 21st century climate based on uncertainties in emissions (without policy) and climate parameters. J Climate 22:5175–5204. doi: 10.1175/2009JCLI2863.1

Webster M, Sokolov AP, Reilly JM, Forest CE, Paltsev S, Schlosser CA, Wang C, Kicklighter DW, Sarofim M, Melillo J, Prinn RJ, Jacoby HD (2011) Analysis of climate policy targets under uncertainty. Climatic Change, 61, 295-320.

Figure 1: Map of greater southern Africa region, highlighting (in white) the ZRB.
Source: http://en.wikipedia.org/wiki/File:Zambezi_river_basin.jpg. Map created from public domain maps available from the University of Texas.

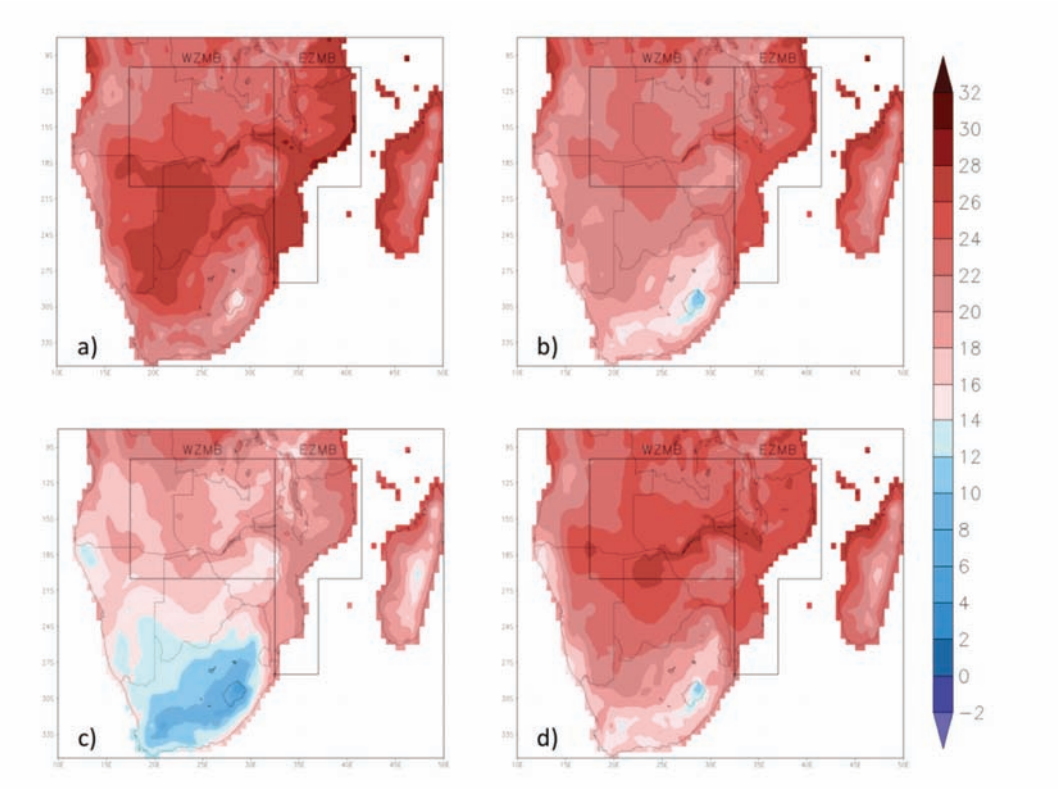

Figure 2: Seasonal averaged (1979-2009) maps of surface air temperature for southern Africa. Results are shown for: a) December-February; b) March-May; c) June-August; and d) September-November. Units are in ˚C. In each frame, the western Zambezi River Basin (WZMB) and eastern Zambezi River Basin (EZMB) averaging domains are outlined, which are used in constructing the HFDs. Temperature data is based on the Climate Research Unit (CRU, Jones et al. 1999) data archive. Infrastructure and Climate Change: Impacts and Adaptations for the Zambezi River Valley.

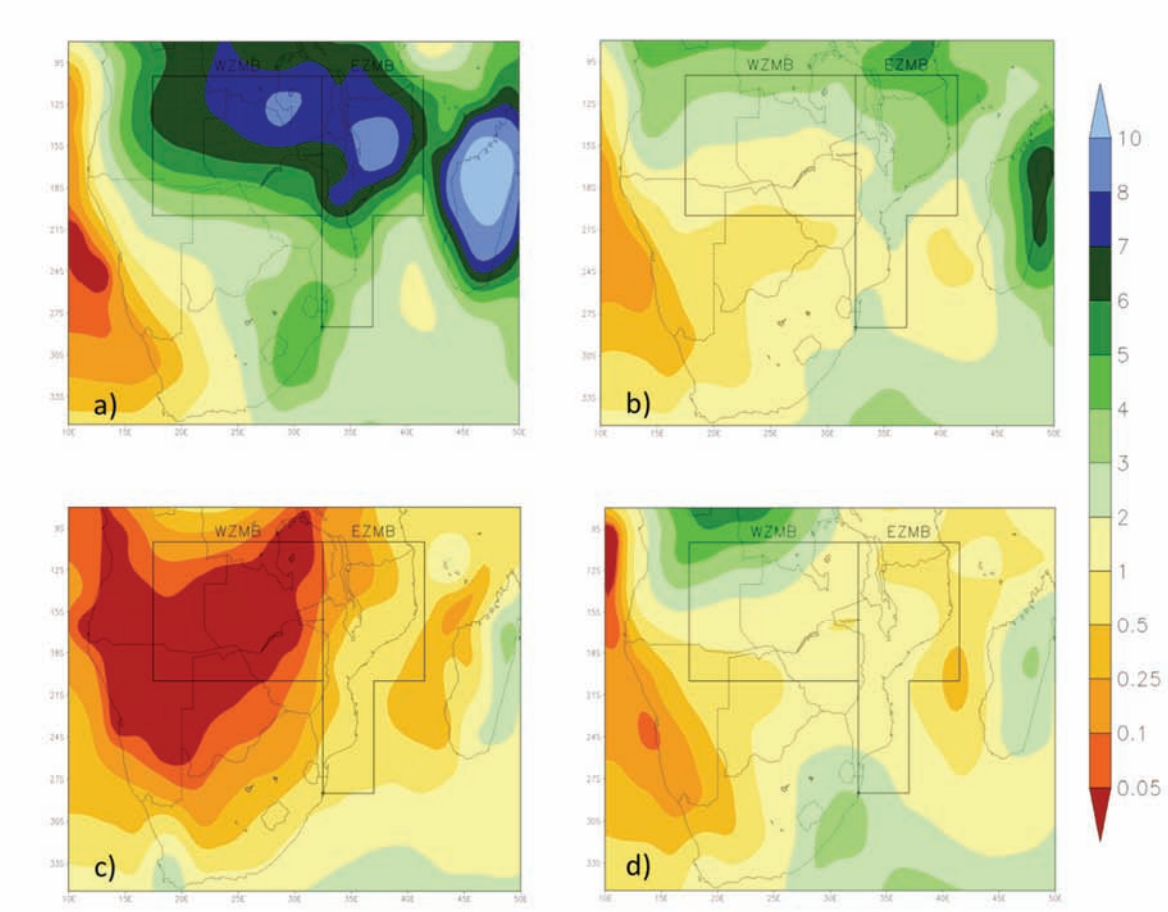

Figure 3: Seasonal averaged maps (1979-2009) of precipitation for southern Africa. Results are shown for: a) December-February; b) March-May; c) June-August; and d) September-November. Units are in mm/day. In each frame, the WZMB and EZMB averaging domains are outlined, which are used in constructing the HFDs. Results are based on the data from the Global Precipitation Climatology Project (GPCP Huffman et al. 2007).

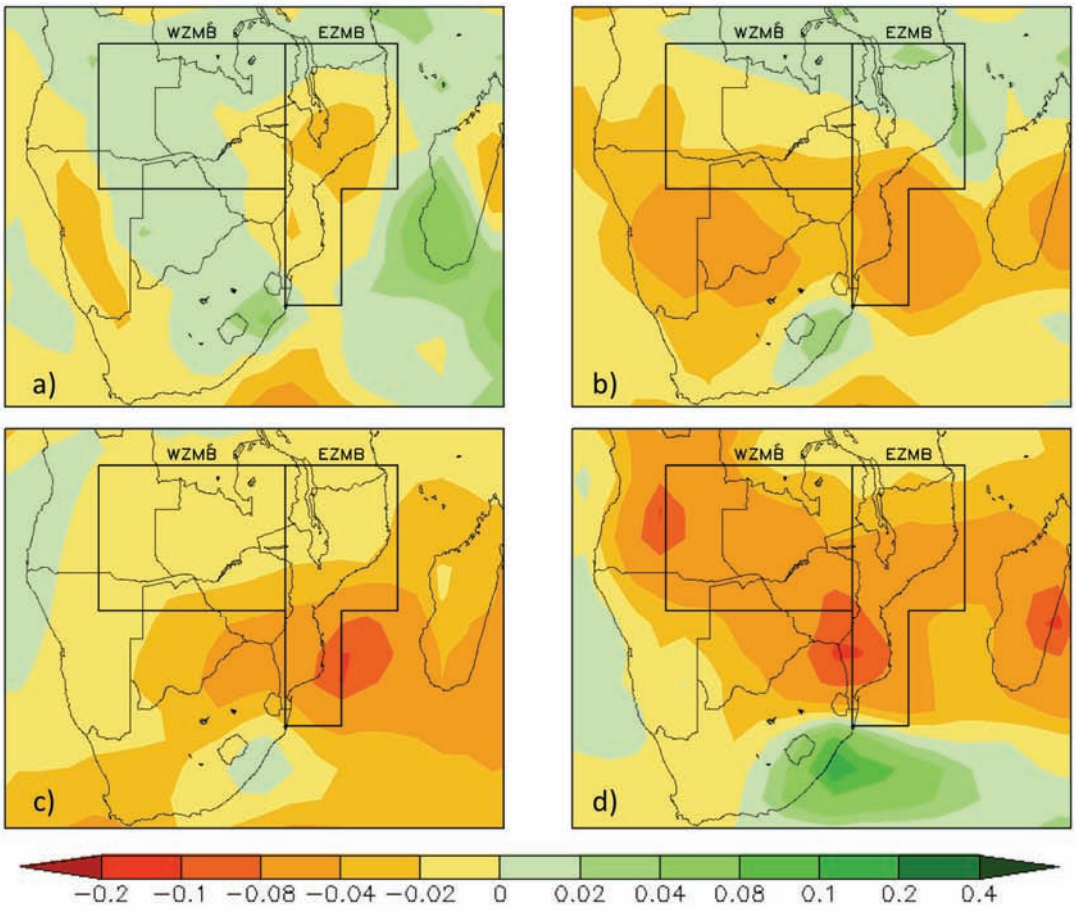

Figure 4: Maps of the transformation coefficients, $dC_{x,y}/dT_{Global}$ (units of K^{-1}) over the southern Africa for precipitation averaged over the results from the IPCC AR4 climate models. Shown are the seasonally averaged pattern shifts averaged for: a) December-February, b) March-May, c) June-August, and d) September-November. In each frame, the WZMB and EZMB averaging domains are outlined, which are used in constructing the HFDs.

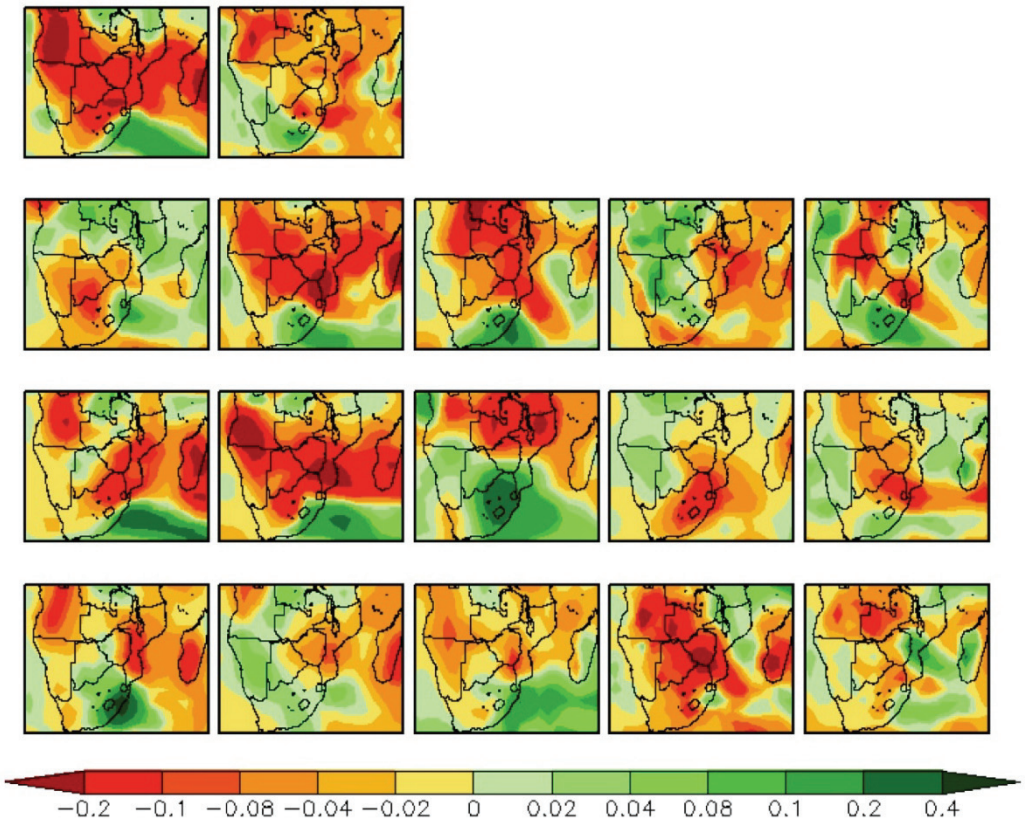

Figure 5: Maps of the transformation coefficients, $dC_{x,y}/dT_{Global}$ (units of K^{-1}) over the southern Africa for precipitation. Shown are the results for each model of the IPCC AR4 collection of the seasonally averaged pattern shifts averaged for September-November.

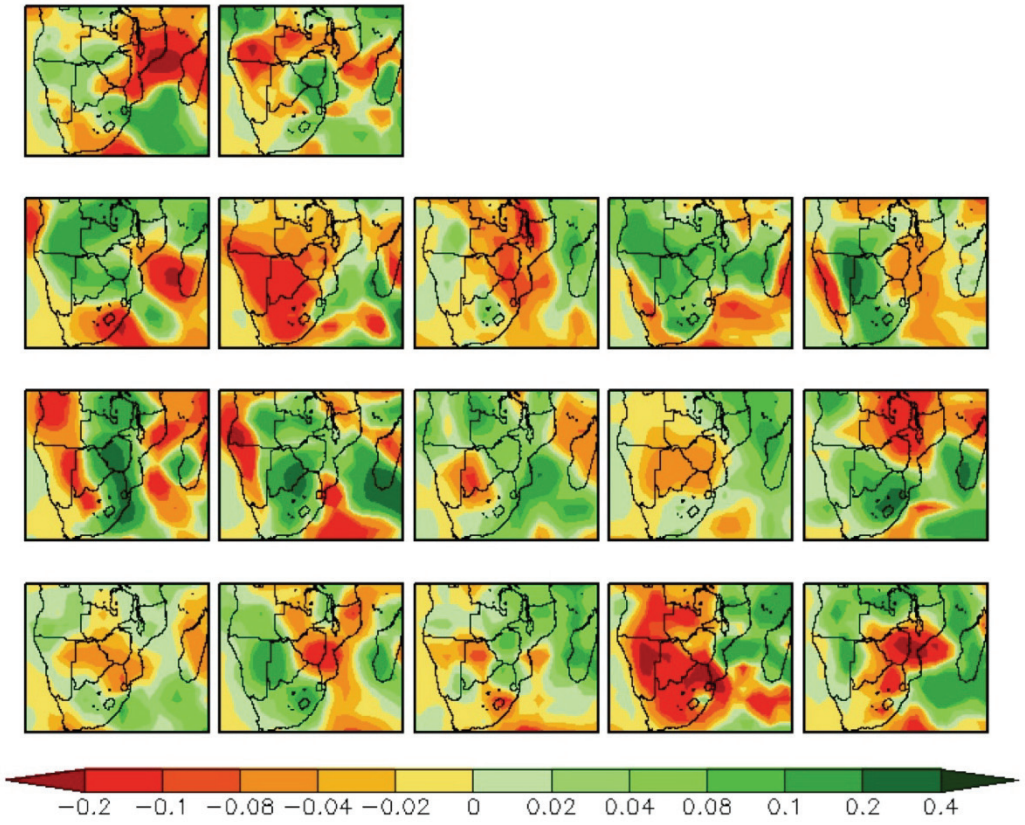

Figure 6: Maps of the transformation coefficients, $dC_{x,y}/dT_{Global}$ (units of K^{-1}) over the southern Africa for precipitation. Shown are the results for each model of the IPCC AR4 collection of the seasonally averaged pattern shifts averaged for December-February.

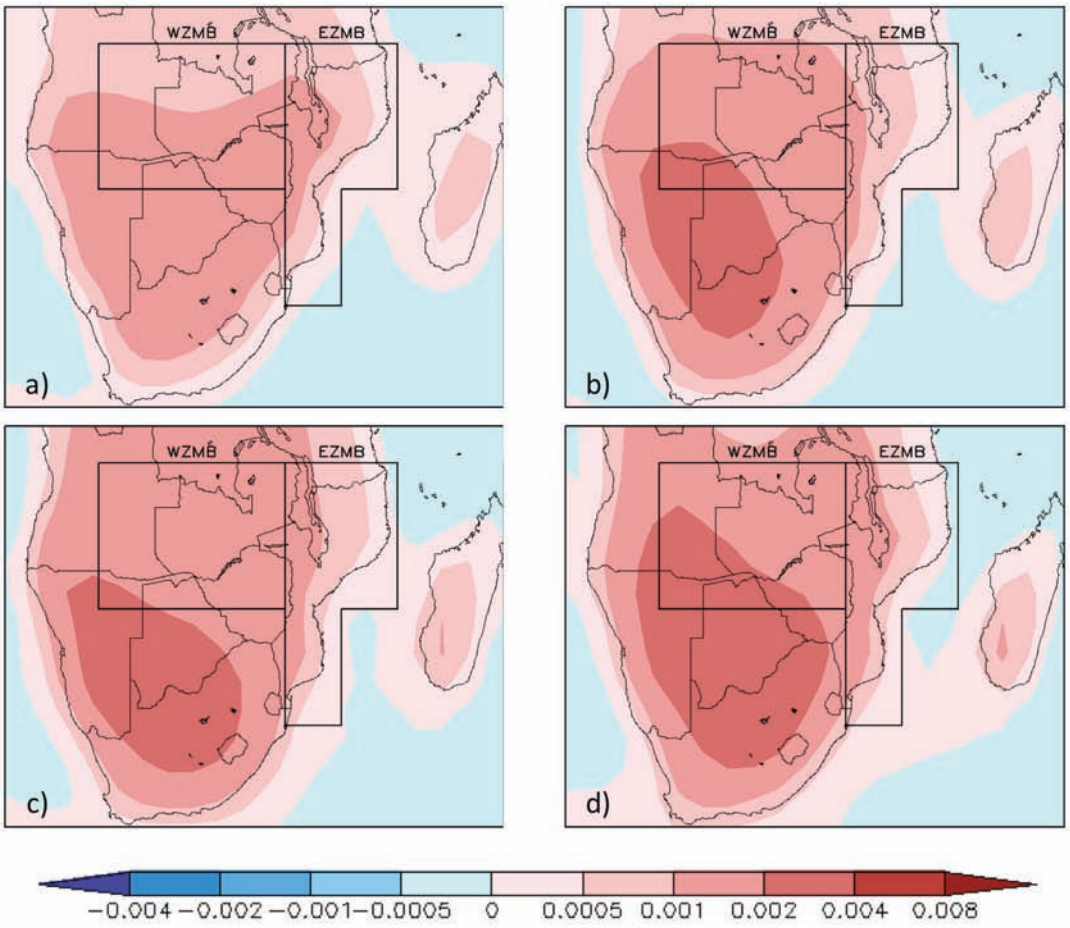

Figure 7: Maps of the transformation coefficients, $dC_{x,y}/dT_{Global}$ (units of K^{-1}) over the southern Africa for surface air temperature based averaged over the results from the IPCC AR4 climate models. Shown are the seasonally averaged pattern shifts averaged for: a) December-February, b) March-May, c) June-August, and d) September-November. . In each frame, the WZMB and EZMB averaging domains are outlined, which are used in constructing the HFDs.

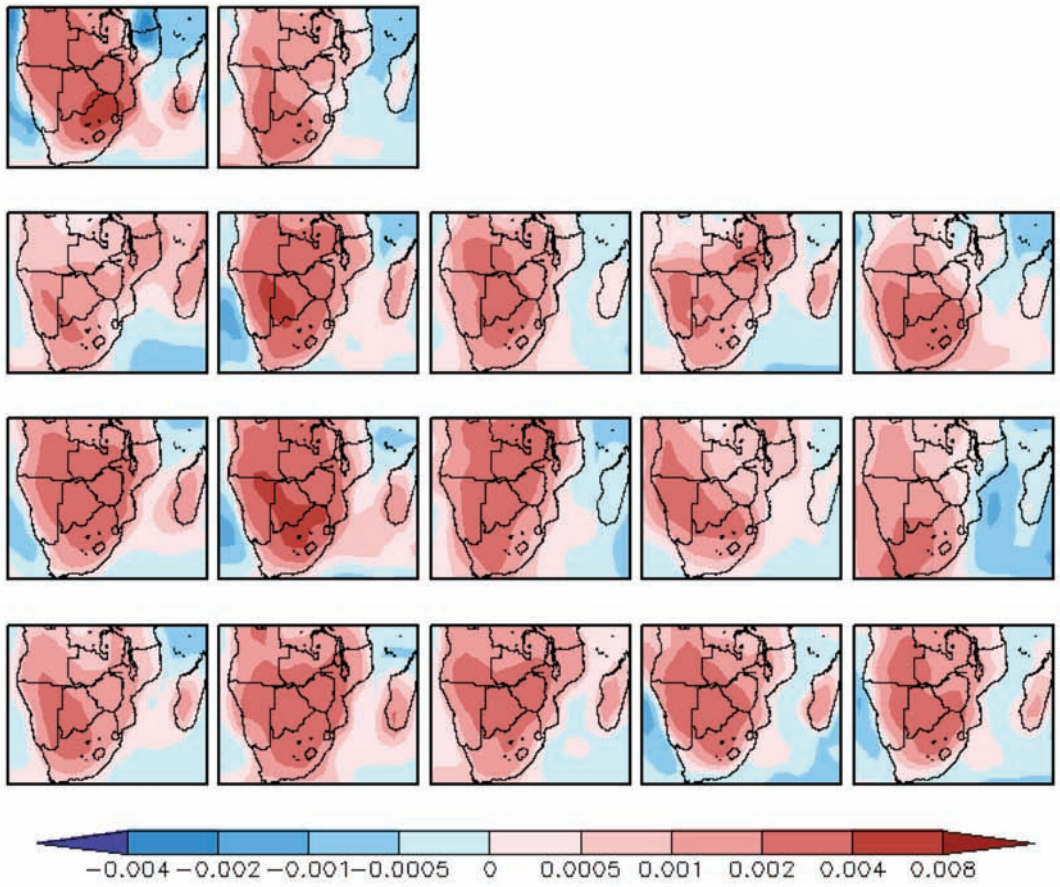

Figure 8: Maps of the transformation coefficients, $dC_{x,y}/dT_{Global}$ (units of K^{-1}) over the southern Africa for surface air temperature. Shown are the results for each model of the IPCC AR4 collection of the seasonally averaged pattern shifts averaged for September-November.

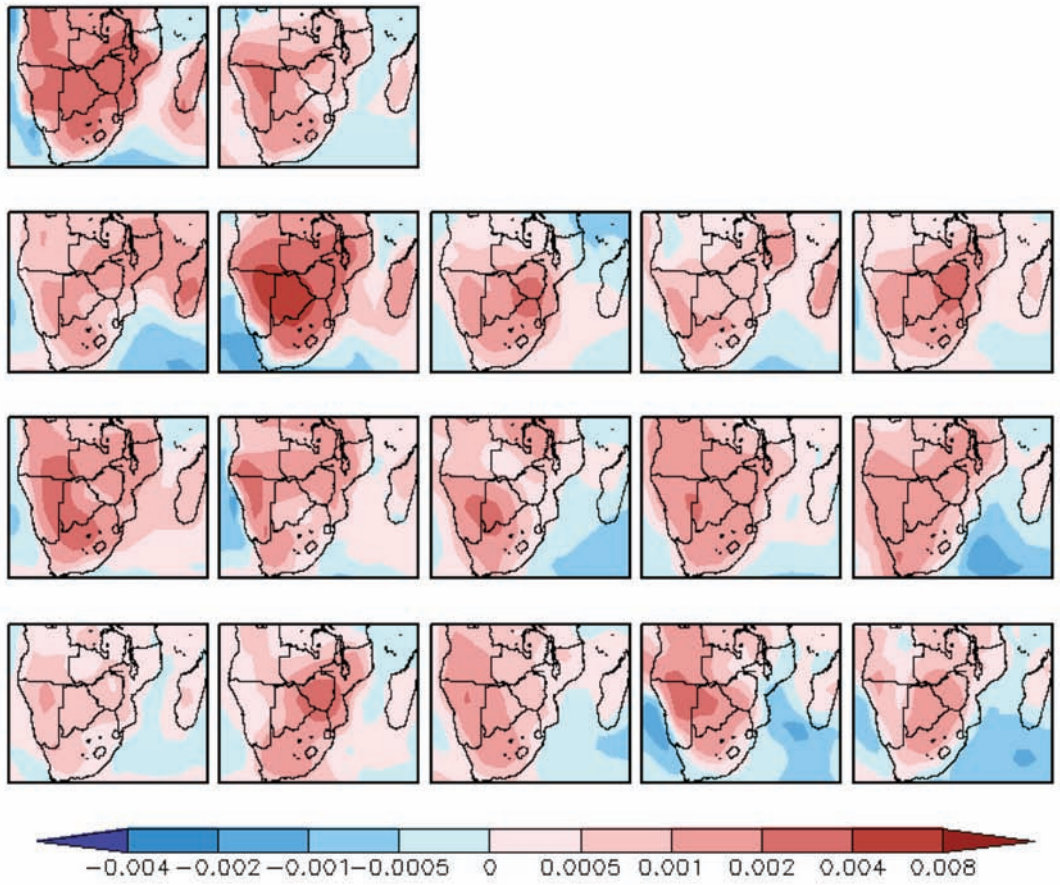

Figure 9: Maps of the transformation coefficients, $dC_{x,y}/dT_{Global}$ (units of K^{-1}) over the southern Africa for surface air temperature. Shown are the results for each model of the IPCC AR4 collection of the seasonally averaged pattern shifts averaged for December-February.

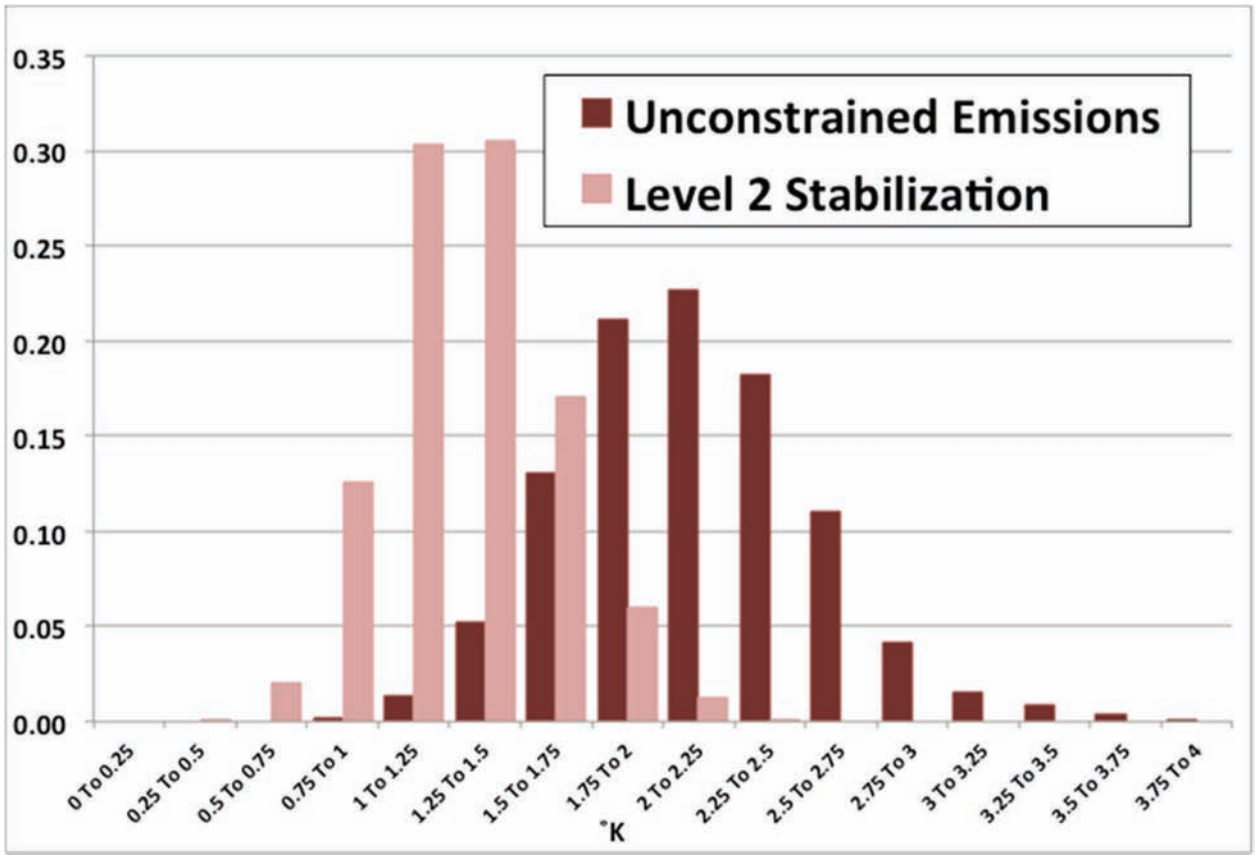

Figure 10: HFDs of decadal averaged September-November (SON) mean surface air temperature (T_a) change (with respect to the last decade of the 20th century). The changes are area averaged for the WZMB. Shown are the decadal-averaged changes at 2050, based on the no-policy IGSM ensemble simulation (dark red bars) and the Level 2 stabilization scenario (light red bars).

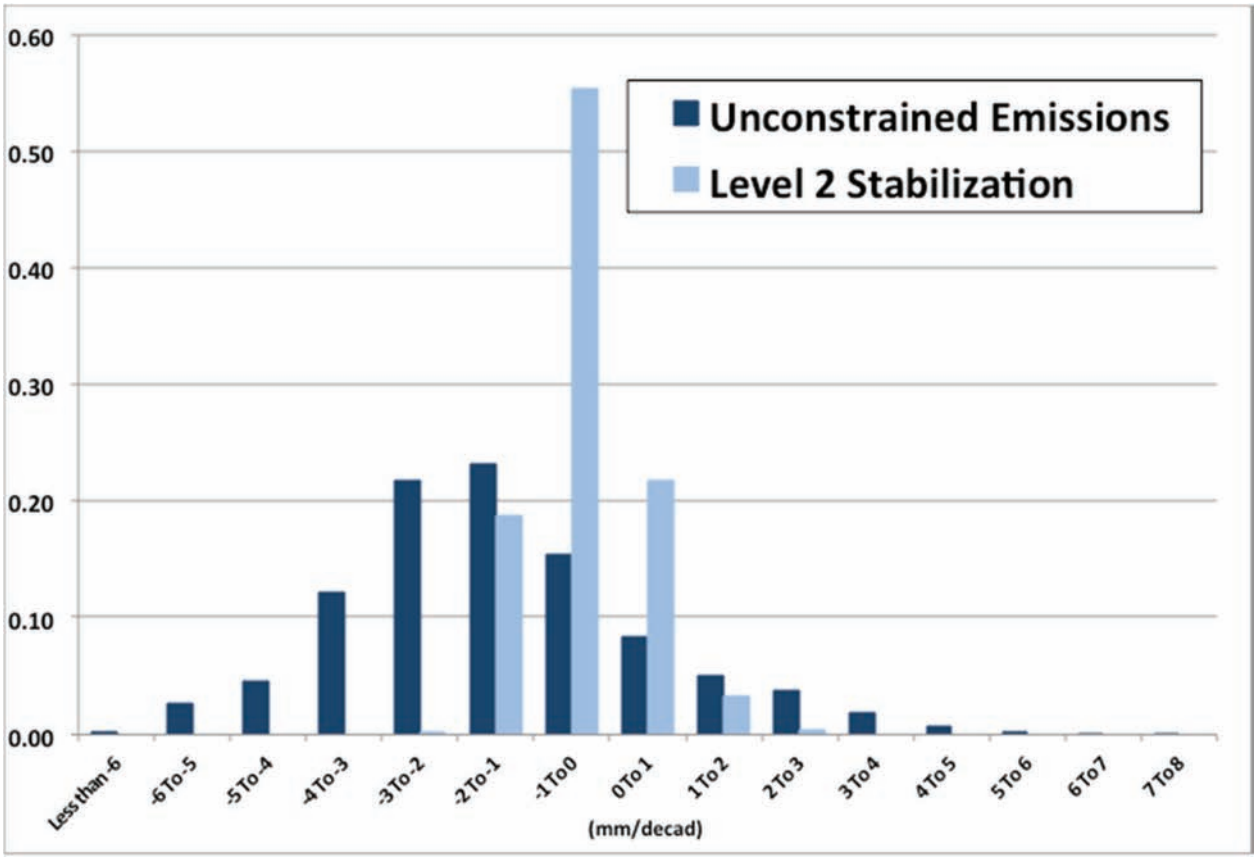

Figure 11: HFDs of decadal averaged September-November (SON) mean precipitation change (with respect to the last decade of the 20th century). The changes are area averaged for the WZMB. Shown are the decadal-averaged changes at 2050, based on the no-policy IGSM ensemble simulation (dark blue bars) and the Level 2 stabilization scenario (light blue bars).

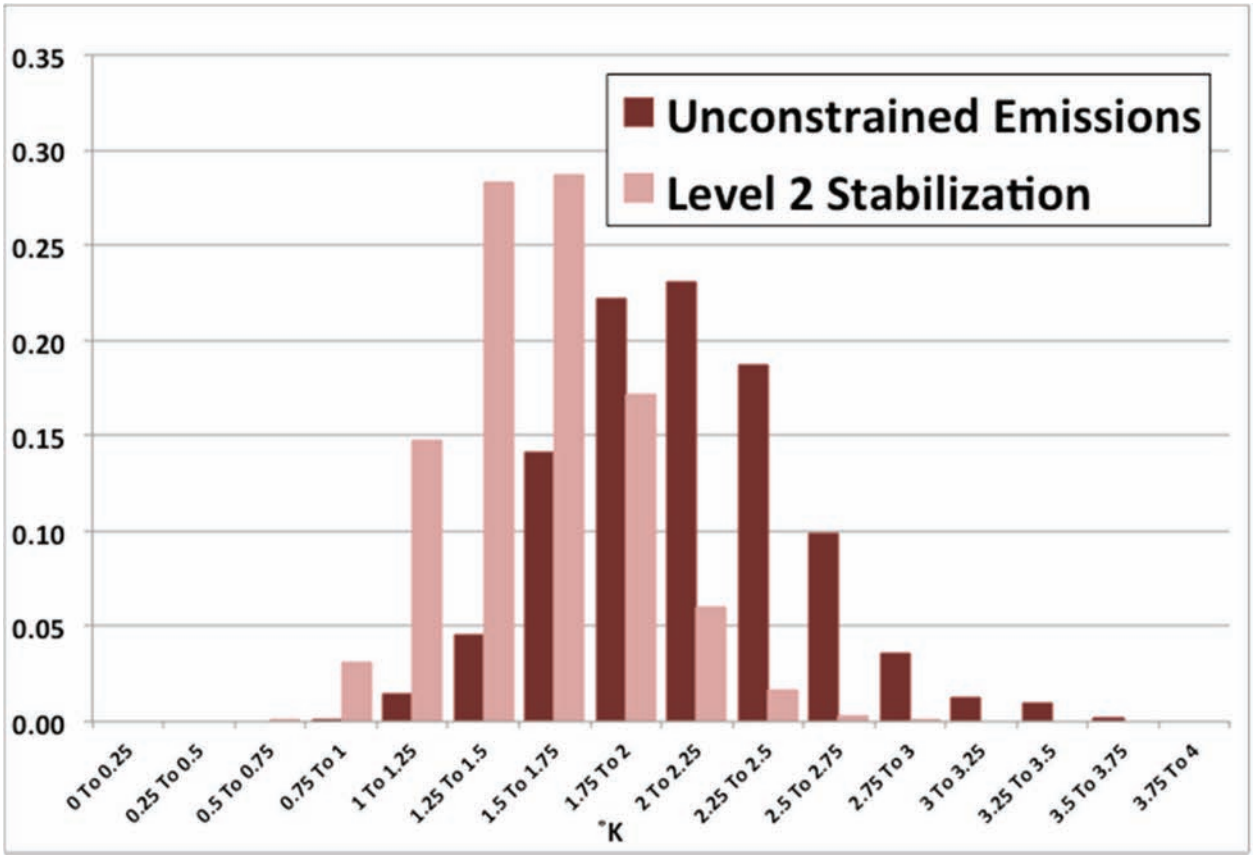

Figure 12: HFDs of decadal averaged December-February (DJF) mean surface air temperature (T_a) change (with respect to the last decade of the 20th century). The changes are area averaged for the WZMB. Shown are the decadal-averaged changes at 2050, based on the no-policy IGSM ensemble simulation (dark red bars) and the Level 2 stabilization scenario (light red bars).

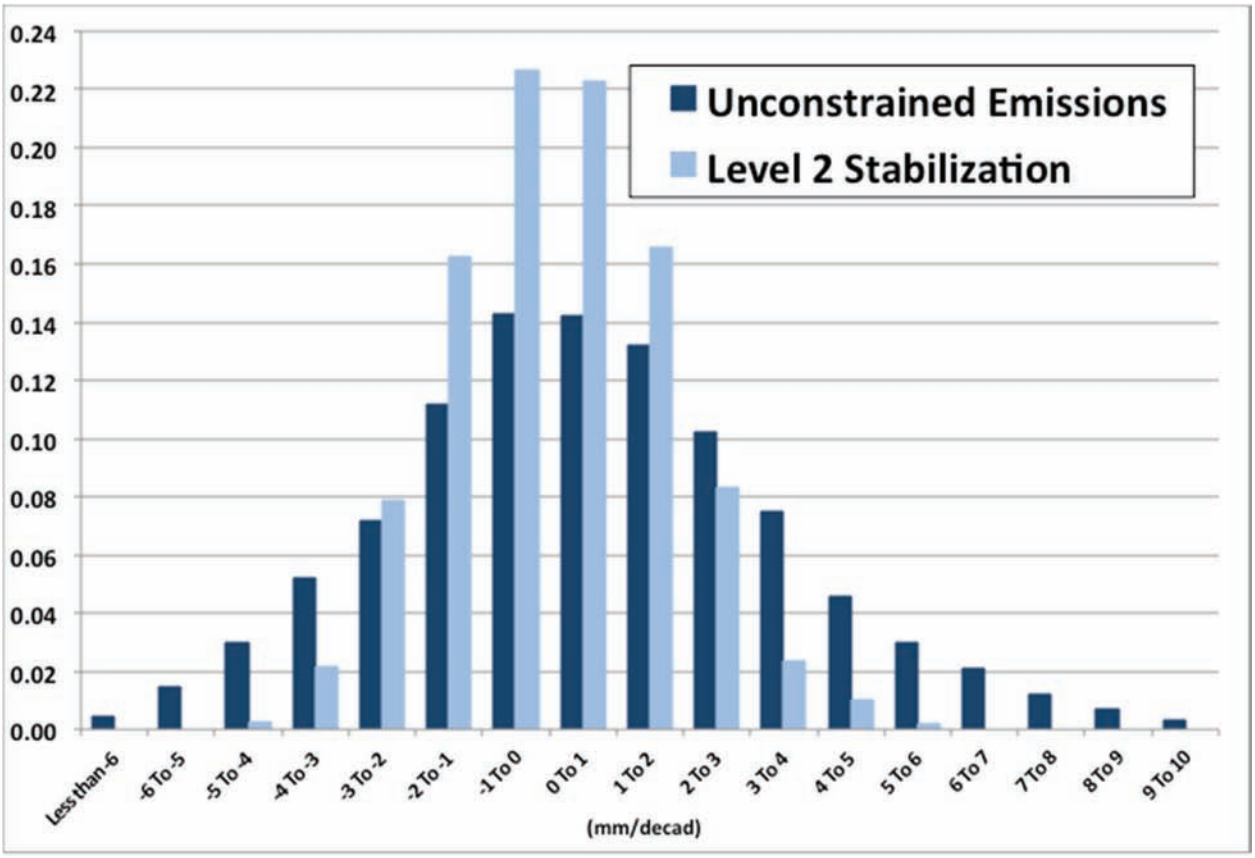

Figure 13: HFDs of decadal averaged December-February (DJF) mean precipitation change (with respect to the last decade of the 20th century). The changes are area averaged for the WZMB. Shown are the decadal-averaged changes at 2050, based on the no-policy IGSM ensemble simulation (dark blue bars) and the Level 2 stabilization scenario (light blue bars).

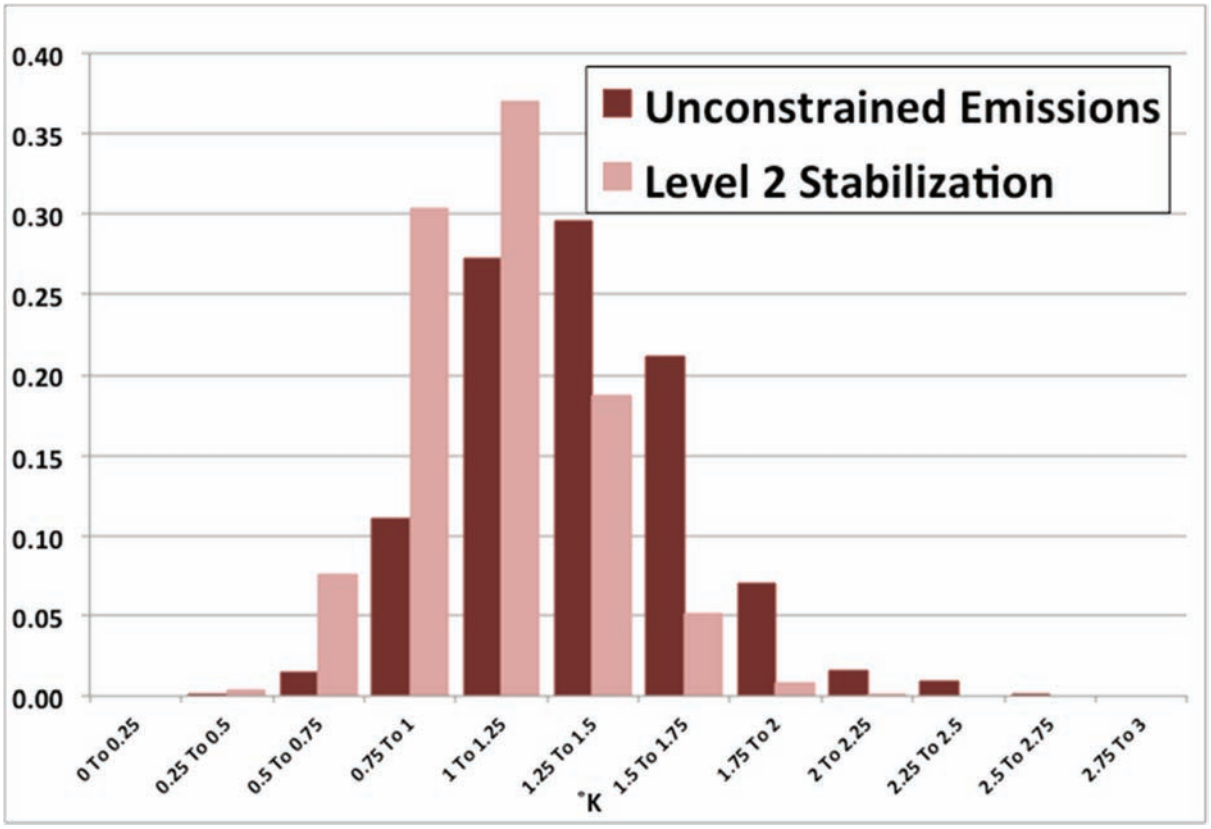

Figure 14: HFDs of decadal averaged December-February (DJF) mean surface air temperature (T_a) change (with respect to the last decade of the 20th century). The changes are area averaged for the EZMB. Shown are the decadal-averaged changes at 2050, based on the no-policy IGSM ensemble simulation (dark red bars) and the Level 2 stabilization scenario (light red bars).

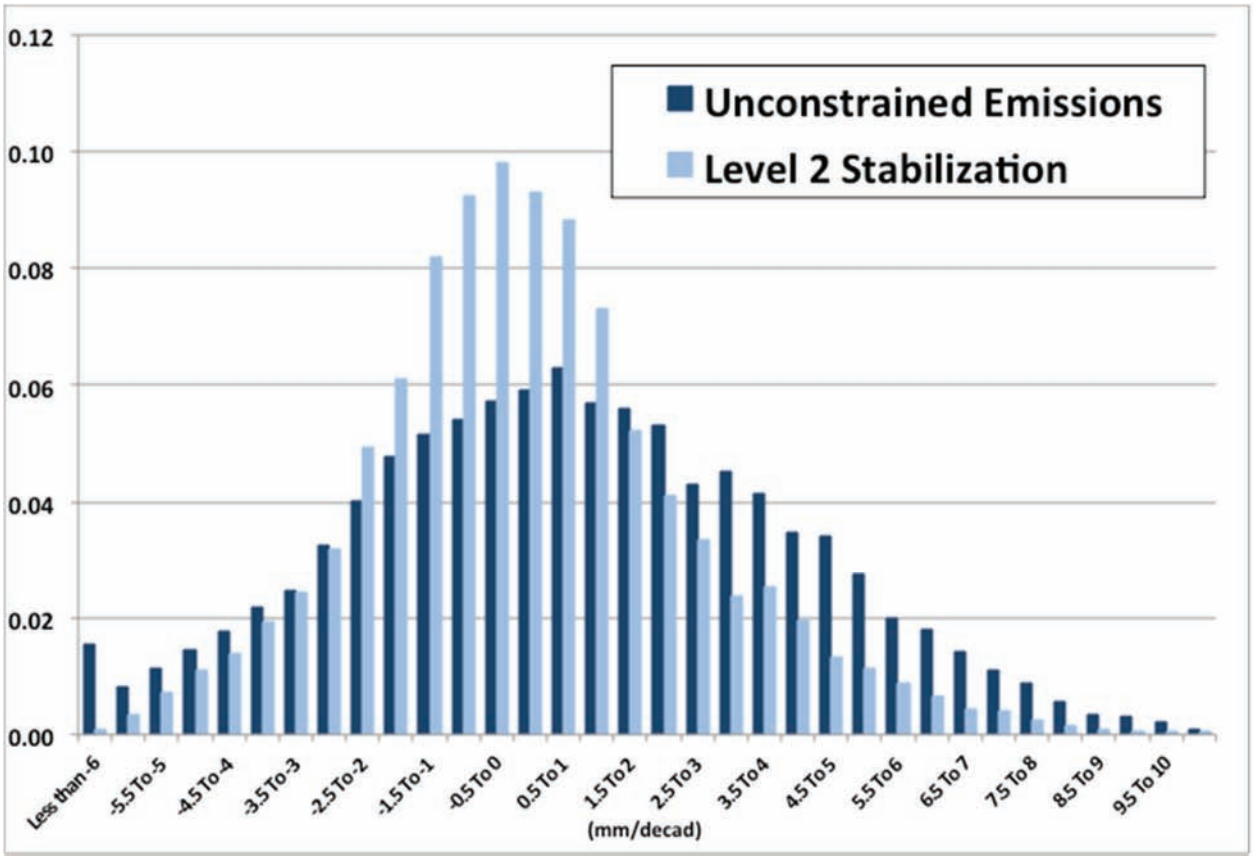

Figure 15: HFDs of decadal averaged December-February (DJF) mean precipitation change (with respect to the last decade of the 20th century). The changes are area averaged for the EZMB. Shown are the decadal-averaged changes at 2050, based on the no-policy IGSM ensemble simulation (dark blue bars) and the Level 2 stabilization scenario (light blue bars).

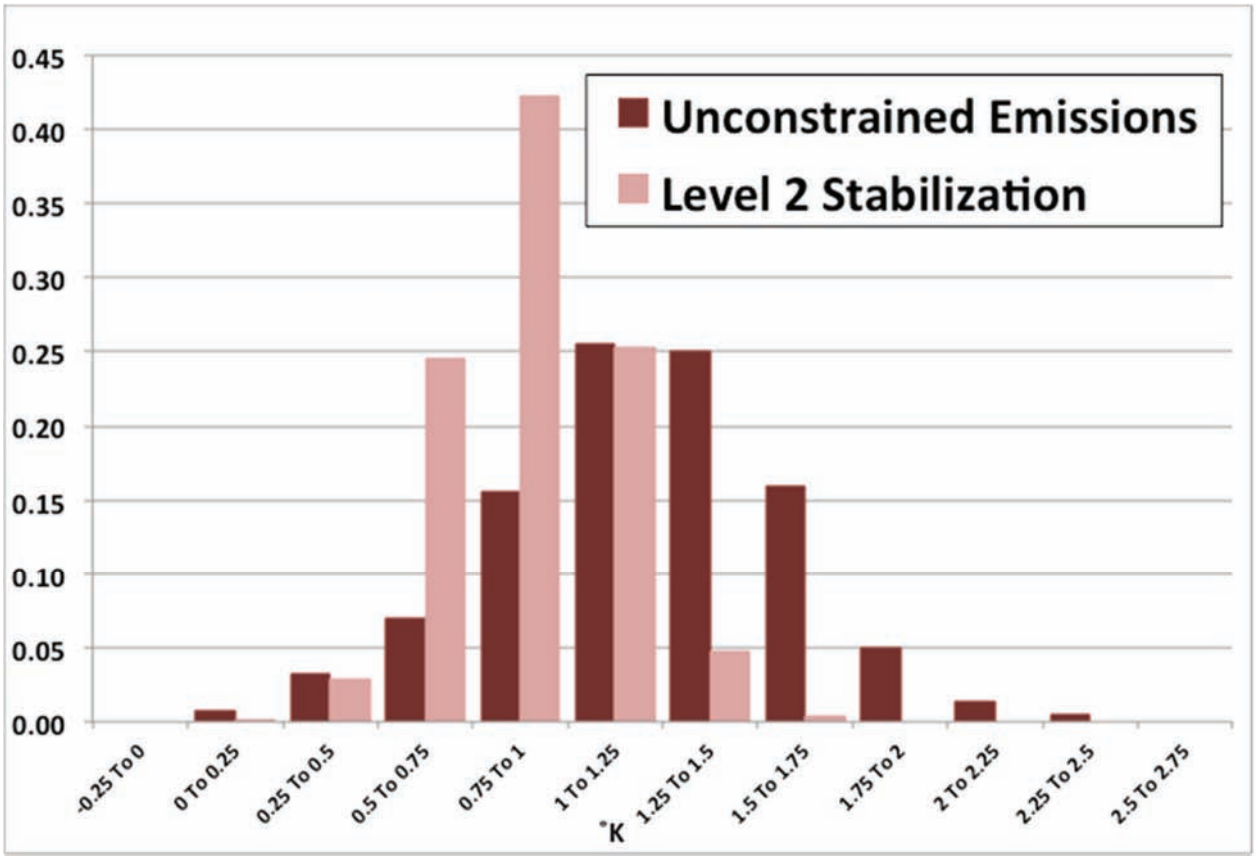

Figure 16: HFDs of decadal averaged September-November (SON) mean surface air temperature (T_a) change (with respect to the last decade of the 20th century). The changes are area averaged for the EZMB. Shown are the decadal-averaged changes at 2050, based on the no-policy IGSM ensemble simulation (dark red bars) and the Level 2 stabilization scenario (light red bars).

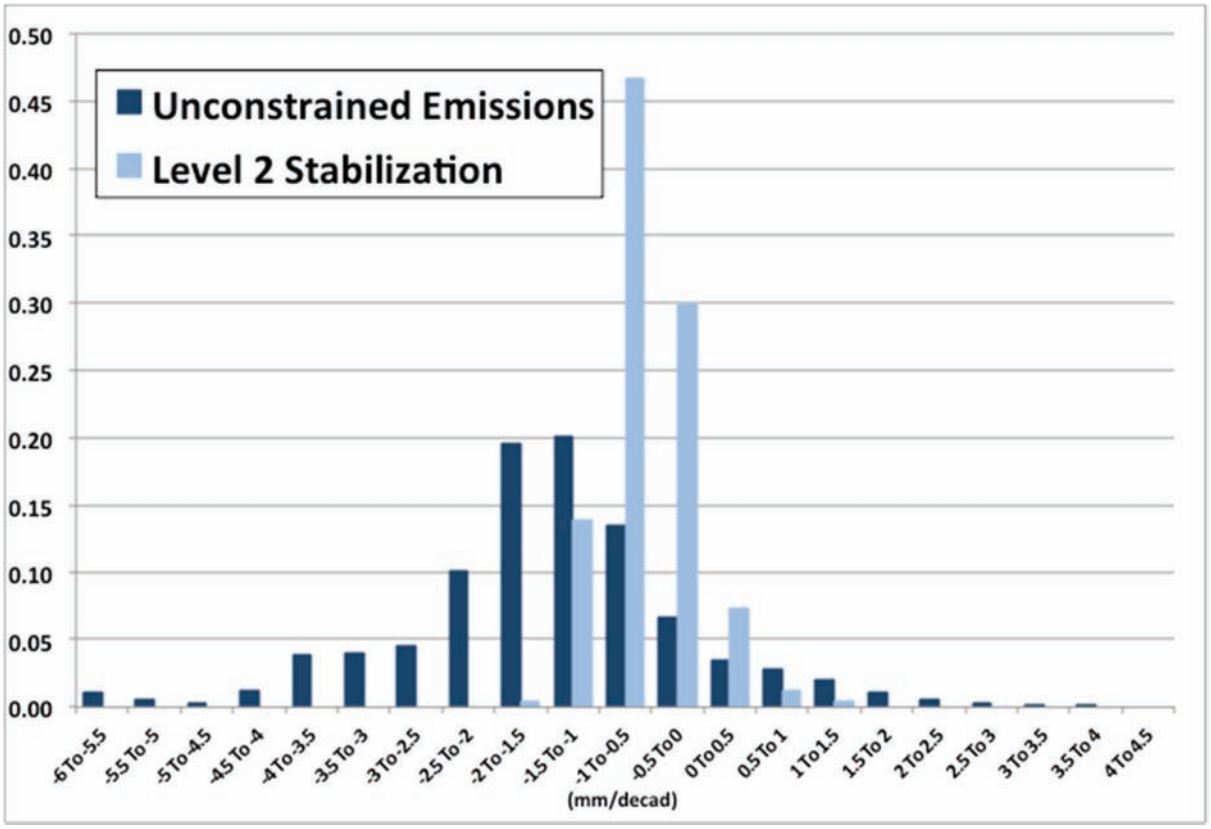

Figure 17: HFDs of decadal averaged September-November (SON) mean precipitation change (with respect to the last decade of the 20th century). The changes are area averaged for the EZMB. Shown are the decadal-averaged changes at 2050, based on the no-policy IGSM ensemble simulation (dark blue bars) and the Level 2 stabilization scenario (light blue bars).